Description of the superdeformed rotational band in ^{40}Ca with a shell-model-like approach

F. Wang (王枫),[1] Z. Shi (施智),[2] and X. W. Xia (夏学伟)[3,*]

[1]*Department of Radiation Oncology, Ruijin Hospital, Shanghai Jiaotong University School of Medicine, Shanghai 200025, China*

[2]*School of Physics, Beihang University, Beijing 100191, China*

[3]*School of Physics and Electronic Engineering, Center for Computational Sciences, Sichuan Normal University, Chengdu 610068, China*

(Received 1 December 2019; revised 17 May 2020; accepted 14 July 2020; published 28 July 2020)

The superdeformed rotational band in ^{40}Ca is investigated in the framework of a shell-model-like approach based on cranking covariant density functional theory, in which the pairing correlations are treated with conserved particle number. A superdeformed state is obtained at the deformation $(\beta, \gamma) = (0.70, 9^\circ)$ even though the depth of the superdeformation minimum is only about 0.2 MeV. With increasing rotational frequency, the potential around the superdeformed minimum becomes deeper. This indicates that the superdeformed state becomes more stable with increasing rotational frequency. Besides, the experimental data are well reproduced by the theoretical calculations with pairing correlations. Pairing correlations are important for the states with $I \leqslant 10\hbar$ in the superdeformed rotational band of ^{40}Ca in reproducing the experimental energy spectrum and transition quadrupole moments.

DOI: 10.1103/PhysRevC.102.014321

I. INTRODUCTION

Strong nuclear deformations provide an excellent framework to investigate the fundamental properties of quantum many-body systems. Experiments have provided evidence in heavy nuclei for the existence of the so-called superdeformation, i.e., strong deformation with width-to-length ratio of 1 : 2. Since the first experimental evidence of the superdeformed rotational band in ^{152}Dy [1], more than 300 superdeformed rotational bands have been identified in different mass regions [2], making it a hot topic in nuclear structure.

Nowadays, the interest in the investigation of superdeformation has transferred to the light mass region. There are many interesting aspects of the superdeformed nuclei in the light mass region [3]: (i) There exist spherical and superdeformed magic numbers with similar particle number. (ii) There exist strong links between the normal (spherical) and superdeformed states, therefore the assignments of spin and parity for the superdeformed rotational band are possible. (iii) This mass region is accessible for various theoretical models, including antisymmetrized molecular dynamics, shell model with large configuration, Monte Carlo shell model, and various density functional theories. Therefore, these nuclei have become ideal test ground for these models.

One example with the above mentioned features is ^{40}Ca. As a double-magic nucleus, the ground-state shape of ^{40}Ca is spherical. Early experimental work has identified the superdeformed rotational band in ^{40}Ca [3]. Various theoretical investigations of the superdeformed rotational band in ^{40}Ca were performed before [4,5] and after this identification [6–10]. In Ref. [6], both the energies and the transition rates up to spin $6\hbar$ for the superdeformed rotational band in ^{40}Ca were correctly reproduced by the Skyrme density functional with particle number and angular momentum projection combined with the generator coordinate method (GCM). The high spin states in the superdeformed rotational band of ^{40}Ca were well reproduced by the cranking density functional theory (DFT), both relativistic [3,9] and nonrelativistic [10,11]. Large-scale shell-model (SM) calculations have also been performed [12–16]. In Ref. [16], with dimension reaching 10^9, large-scale SM calculations were carried out to describe the observed deformed and superdeformed bands. The large-scale SM calculations not only describe the energy levels and the triple coexistence observed in this nucleus but also predict fairly accuracy electromagnetic transition probabilities measured in the decay out of the superdeformed state. The configuration-dependent cranked Nilsson-Strutinsky approach was used to investigated shape coexistence and band structure near the yrast line of the ^{40}Ca in Ref. [17]. Focusing on the $^{12}\mathrm{C} + ^{28}\mathrm{Si}$ molecular bands, the deformed states in ^{40}Ca were investigated with a method of antisymmetrized molecular dynamics (AMD) and GCM [18,19]. By means of the random phase approximation (RPA), calculations based on the deformed and cranked deformed Woods-Saxon potentials as well as the Skyrme-Hartree-Fock mean field have been done to study the octupole excitations built on the superdeformed state in ^{40}Ca [20–22]. Using the P + QQ model based on the cranked Hartree-Fock-Bogoliubov method, investigations were carried out particularly for cross-shell excitations in the *sd* and *pf* shells, the roles of the $g_{9/2}$ and $d_{5/2}$ orbits, the effects of nuclear pairing, and the interplay between triaxiality and band termination in Ref. [23]. Besides the band structure, the potential barriers governing the evolution of a rotating nucleus ^{40}Ca have been determined using a generalized liquid drop model [24].

As shown in Ref. [3], at low rotational frequencies, discrepancies between experiment and cranking covariant DFT

*xwxia@sicnu.edu.cn

(CDFT) calculations emerge, indicating the need for pairing. In Ref. [9], cranking relativistic Hartree-Bogoliubov (CRHB) calculations were performed. In these calculations the Lipkin-Nogami method was employed for an approximate particle number projection and the Gogny D1S force was used in the pairing channel. The presence of pairing correlations led to an additional binding for the low-spin area. The shell-model-like approach (SLAP) [25,26] is a method that treats pairing correlations with conserved particle number and blocking effects exactly by diagonalizing the many-body Hamiltonian in a many-particle configuration (MPC) space. Since being promoted in 1983, SLAP has been widely used in different models. For example, based on the phenomenological cranking Nilsson model, extensive applications to the odd-even differences in moments of inertia [27,28], identical bands [29,30], the nuclear pairing phase transition [31], antimagnetic rotation [32,33], and high-K rotational bands in the rare-earth [34–40] and actinide nuclei [41–44] have been performed. Based on the microscopic CDFT, SLAP was first adopted to study the ground-state properties and low-lying excited states for Ne isotopes [26]. In Ref. [45], an extension to include the temperature was implemented to study the heat capacity. Recently, SLAP has been implemented in the cranking CDFT and applied to the investigations of the band crossing mechanism and shape evolution in ^{60}Fe [46] and the antimagnetic rotation band in ^{101}Pd [47].

In the present paper, the superdeformed rotational band in ^{40}Ca will be investigated in the framework of SLAP based on the cranking CDFT (referred to as cranking CDFT-SLAP). The properties of the superdeformed state in ^{40}Ca with rotation will also be investigated, and the pairing effect in the superdeformed rotational band will be explored. The calculated energy spectra, moments of inertia, and transition quadrupole moments will be compared with the experimental data.

The paper is organized as follows. In Sec. II, the theoretical frameworks for the cranking CDFT and SLAP are briefly presented. The numerical details are given in Sec. III. In Sec. IV, the potential energy surface, single-particle levels, energy spectra, moments of inertia, and transition quadrupole moments calculated by the cranking CDFT-SLAP are presented and compared with the data. A short summary is given in Sec. V.

II. THEORETICAL FRAMEWORK

The effective Lagrangian density for the point-coupling covariant density functional is written as [48,49]

$$\begin{aligned}\mathcal{L} &= \mathcal{L}^{\text{free}} + \mathcal{L}^{\text{4f}} + \mathcal{L}^{\text{hot}} + \mathcal{L}^{\text{der}} + \mathcal{L}^{\text{em}} \\ &= \bar{\psi}(i\gamma_\mu\partial^\mu - m)\psi \\ &\quad - \frac{1}{2}\alpha_S(\bar{\psi}\psi)(\bar{\psi}\psi) - \frac{1}{2}\alpha_V(\bar{\psi}\gamma_\mu\psi)(\bar{\psi}\gamma^\mu\psi) \\ &\quad - \frac{1}{2}\alpha_{TV}(\bar{\psi}\vec{\tau}\gamma_\mu\psi)(\bar{\psi}\vec{\tau}\gamma^\mu\psi) \\ &\quad - \frac{1}{3}\beta_S(\bar{\psi}\psi)^3 - \frac{1}{4}\gamma_S(\bar{\psi}\psi)^4 - \frac{1}{4}\gamma_V[(\bar{\psi}\gamma_\mu\psi)(\bar{\psi}\gamma^\mu\psi)]^2 \\ &\quad - \frac{1}{2}\delta_S\partial_\nu(\bar{\psi}\psi)\partial^\nu(\bar{\psi}\psi) - \frac{1}{2}\delta_V\partial_\nu(\bar{\psi}\gamma_\mu\psi)\partial^\nu(\bar{\psi}\gamma^\mu\psi) \\ &\quad - \frac{1}{2}\delta_{TV}\partial_\nu(\bar{\psi}\vec{\tau}\gamma_\mu\psi)\partial^\nu(\bar{\psi}\vec{\tau}\gamma^\mu\psi) \\ &\quad - \frac{1}{4}F^{\mu\nu}F_{\mu\nu} - e\frac{1-\tau_3}{2}\bar{\psi}\gamma^\mu\psi A_\mu, \end{aligned} \tag{1}$$

which includes the free nucleon term $\mathcal{L}^{\text{free}}$, the four-fermion point-coupling terms $\mathcal{L}^{\text{4f}}$, the higher-order terms $\mathcal{L}^{\text{hot}}$ responsible for the medium effects, the gradient terms $\mathcal{L}^{\text{der}}$ simulating the effects of finite range, and the electromagnetic interaction terms $\mathcal{L}^{\text{em}}$.

To describe the nuclear rotation, the effective Lagrangian (1) is transformed into a rotating frame with a constant rotational frequency ω_x around the x axis [50–52]. The equation of motion for the nucleons derived from the rotating Lagrangian is written as

$$\hat{h}_0\psi_\mu = (\hat{h}_{\text{s.p.}} + \hat{h}_{\text{c}})\psi_\mu = \varepsilon_\mu\psi_\mu, \tag{2}$$

with

$$\hat{h}_{\text{s.p.}} = \boldsymbol{\alpha}\cdot(-i\boldsymbol{\nabla} - \boldsymbol{V}) + \beta(m+S) + V^0, \quad \hat{h}_{\text{c}} = -\omega_x\cdot\hat{j}_x, \tag{3}$$

where $\hat{j}_x = \hat{l}_x + \frac{1}{2}\Sigma_x$ is x component of the total angular momentum of the nucleon spinors, and ε_μ represents the single-particle Routhians for nucleons. $S(\boldsymbol{r})$ and $V^\mu(\boldsymbol{r})$ are the relativistic fields.

The pairing correlations are treated by the shell-model-like approach. The cranking many-body Hamiltonian with pairing correlations reads

$$\hat{H} = \hat{H}_0 + \hat{H}_{\text{pair}}. \tag{4}$$

The one-body Hamiltonian is written as $\hat{H}_0 = \sum\hat{h}_0$ with $\hat{h}_0$ given in Eq. (2). The monopole pairing Hamiltonian $\hat{H}_{\text{pair}}$ is used,

$$\hat{H}_{\text{pair}} = -G\sum_{\xi,\eta>0}^{\xi\neq\eta}\hat{\beta}^\dagger_\xi\hat{\beta}^\dagger_{\bar{\xi}}\hat{\beta}_{\bar{\eta}}\hat{\beta}_\eta, \tag{5}$$

where G is the effective pairing strength, $\bar{\xi}$ ($\bar{\eta}$) labels the time-reversal state of ξ (η), and $\xi\neq\eta$ means that the self-scattering for the nucleon pairs is forbidden [26].

The idea of cranking CDFT-SLAP is to diagonalize the many-body Hamiltonian in a properly truncated MPC space, which is constructed from the single-particle Routhians from the cranking CDFT. The MPC $|i\rangle$ for an n-particle system can be constructed as [53]

$$|i\rangle = |\mu_1\mu_2\cdots\mu_n\rangle = \hat{b}^\dagger_{\mu_1}\hat{b}^\dagger_{\mu_2}\cdots\hat{b}^\dagger_{\mu_n}|0\rangle. \tag{6}$$

$|\mu\rangle$ denotes the occupied single-particle Routhians obtained from cranking CDFT. The parity π, signature α, and the corresponding configuration energy for each MPC are obtained from the occupied single-particle Routhians.

The eigenstates for the cranking many-body Hamiltonian are obtained by diagonalization in the MPC space,

$$|\Psi\rangle = \sum_i C_i|i\rangle, \tag{7}$$

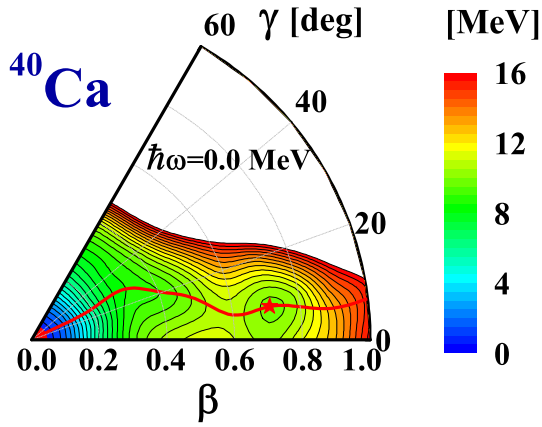

FIG. 1. The potential energy surface calculated by cranking CDFT-SLAP at $\hbar\omega = 0.0$ MeV for ^{40}Ca. The dot and star denote the locations of global and superdeformed minima, respectively. The energy difference between the neighboring contour lines is 0.5 MeV. The red solid line is determined by searching for the energy minimum in the γ direction.

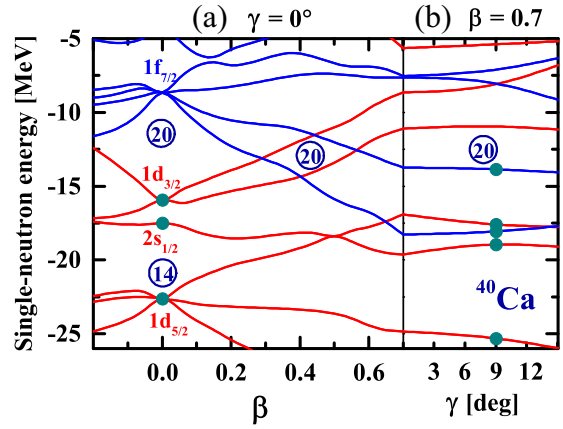

FIG. 2. The neutron single-particle energy levels of ^{40}Ca as functions of the quadrupole deformation β (a) and γ (b). The positive (negative) parity levels are denoted by red (blue) lines.

with C_i the expanding coefficients. The detailed formalisms of cranking CDFT-SLAP can be found in Ref. [46].

III. NUMERICAL DETAILS

In the present cranking CDFT-SLAP calculations for ^{40}Ca, the point-coupling density functional PC-PK1 [48] is used in the particle-hole channel and the monopole pairing interaction is adopted in the particle-particle channel. The equation of motion (2) is solved by expanding the Dirac spinor in terms of the three-dimensional harmonic oscillator basis with 14 major shells. For both neutron and proton, the dimensions of the MPC space are chosen as 1000, which correspond to the energy cutoffs $E_c \approx 22$ and $\approx$23 MeV, respectively. The effective pairing strengths are 1.0 MeV for both neutron and proton by reproducing the experimental odd-even mass differences. Increasing the number of major shells from 14 to 16, the change of the total energy is within 0.1%. Increasing the dimension of the MPC space from 1000 to 1500 and adjusting the effective pairing strength accordingly, the change of the total energy is within 0.1%. In the present calculation, there is no free parameter.

IV. RESULTS AND DISCUSSION

A. Potential energy surface

To confirm the existence of the superdeformed state in ^{40}Ca, the potential energy surface calculated by the cranking CDFT-SLAP at $\hbar\omega = 0.0$ MeV is plotted in Fig. 1. The red solid line in the potential energy surface is the adiabatic energy curve that determined by searching for the energy minimum in the γ direction.

As can be seen in the potential energy surface, the ground state of ^{40}Ca is spherical. Apart from that, a superdeformed minimum is found around the deformation $(\beta, \gamma) = (0.7, 9^\circ)$, which is in agreement with the upper limit of the experimental data for the superdeformed state in ^{40}Ca, $\beta = 0.59^{+0.11}_{-0.07}$ [3].

B. Single-particle levels

To understand the microscopic mechanism of the shape evolution better, in Fig. 2, the neutron single-particle energy levels of ^{40}Ca as functions of the quadrupole deformation β and γ for the adiabatic potential energy curve are shown.

As can be seen from Fig. 2(a), with the increase of quadrupole deformation β, the last occupied twofold degenerate orbit changes from $1d_{3/2}$ at the spherical ground state to $1f_{7/2}$ at the normal deformed state around $\beta \approx 0.4$, and a clear energy gap can be seen. Therefore, the neutron configuration for the normal deformed state is $1f_{7/2}^2 1d_{3/2}^{-2}$. With increasing β, from the normal deformed state to the superdeformed state, another occupied $1d_{3/2}$ orbit changes to $1f_{7/2}$. Hence, the neutron configuration for the superdeformed state in ^{40}Ca is $1f_{7/2}^4 1d_{3/2}^{-4}$.

As shown in Fig. 2(b), the neutron single-particle energy levels change smoothly with γ, indicating that the superdeformed state is soft with γ.

Apart from the Coulomb shift in energy, the proton single-particle energy levels are similar to those of neutron shown in Fig. 2. Therefore, the configurations for the normal deformed and superdeformed states are $\nu(1f_{7/2}^2 1d_{3/2}^{-2}) \otimes \pi(1f_{7/2}^2 1d_{3/2}^{-2})$ and $\nu(1f_{7/2}^4 1d_{3/2}^{-4}) \otimes \pi(1f_{7/2}^4 1d_{3/2}^{-4})$. These are consistent with famous four-particle–four-hole (4p4h) and eight-particle–eight-hole (8p8h) configurations [3].

C. Potential energy curve

Next, we take rotation into account. The rotational properties for the spherical (0p0h), normal deformed (4p4h), and superdeformed (8p8h) configurations have been investigated at the rotational frequencies $\hbar\omega = 0.0$, 0., 5, 1.0, 1.5, and 2.0 MeV, as functions of the quadrupole deformation β, as shown in Fig. 3.

At the rotational frequencies $\hbar\omega = 0.0$, 0.5, and 1.0 MeV, the energy differences between the global and local minima

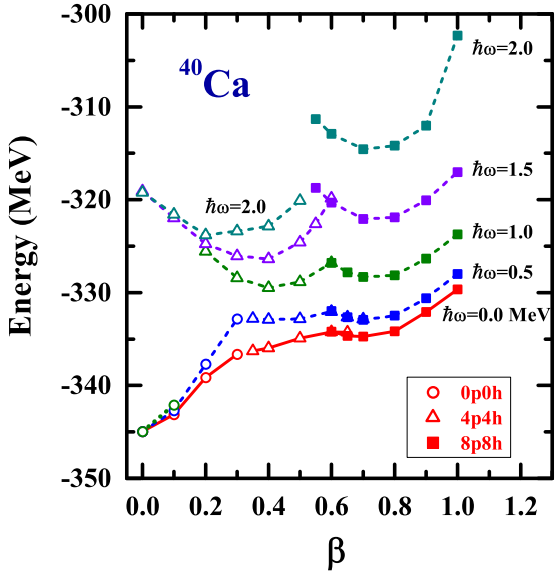

FIG. 3. The potential energy curve for the spherical (0p0h), normal deformed (4p4h), and superdeformed (8p8h) configurations at rotational frequencies $\hbar\omega = 0.0$, 0.5, 1.0, 1.5, and 2.0 MeV, as functions of quadrupole deformation β.

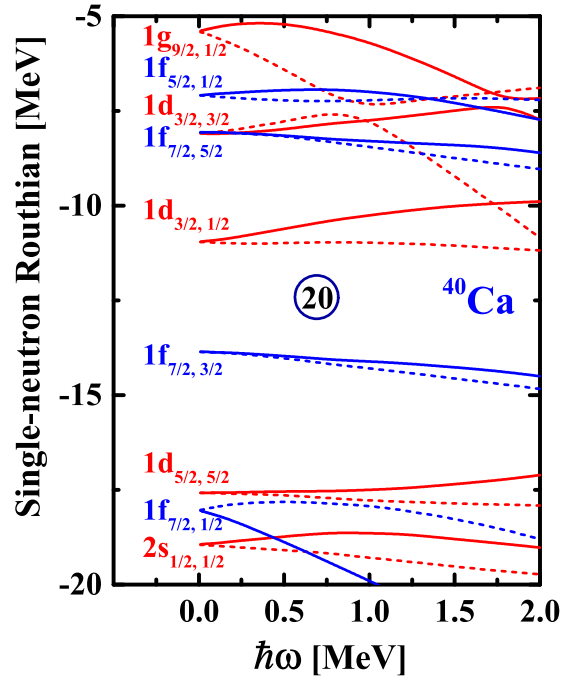

FIG. 4. The neutron single-particle Routhians for the superdeformed state in ^{40}Ca as functions of rotational frequency $\hbar\omega$. The positive (negative) parity levels are denoted by red (blue) lines. The signature $\alpha = +1/2$ $(-1/2)$ levels are denoted by solid (dashed) lines.

are 10.2, 12.0, and 16.6 MeV, respectively. At the rotational frequencies $\hbar\omega = 1.5$ and 2.0 MeV, the energy differences between the global and local minima are 4.3 and 9.5 MeV, respectively. With increasing rotational frequency, the global minimum changes from spherical to normal deformed. For the superdeformed state, the depth of the superdeformed minimum is only about 0.2 MeV at $\hbar\omega = 0.0$ MeV. With increasing rotational frequency, the potential around the superdeformed minimum will become deeper, indicating that the superdeformed state will become more stable.

D. Single-particle Routhian

In order to analyze the superdeformed state under rotation, the neutron single-particle Routhians for the superdeformed state in ^{40}Ca as functions of the rotational frequency are shown in Fig. 4.

As shown in Fig. 4, the superdeformation configuration remains unchanged with increasing rotational frequency. A clear energy gap above $N = 20$ is seen. With increasing rotational frequency, the energy gap increases from about 2.9 MeV at $\hbar\omega = 0.0$ MeV to about 3.5 MeV at $\hbar\omega = 2.0$ MeV. This indicates that, in the present frequency region, the superdeformed state will become more stable with increasing rotational frequency. This is consistent with the potential energy curve of the superdeformed state shown in Fig. 3.

E. Comparison with the experimental data

To show the importance of pairing correlations, the calculated energy spectrum, moments of inertia, and transition quadrupole moments by cranking CDFT-SLAP with and without pairing correlations are compared with the available data and results from other methods.

1. Energy spectrum and pairing energy

In Fig. 5(a), the energy spectra as functions of spin for the superdeformed rotational band in ^{40}Ca calculated by cranking CDFT-SLAP with and without pairing are compared with the available data [3] and the cranking relativistic mean-field (CRMF) results with the NL3 effective interaction [3]. It is noted that the $I = 16\hbar$ state is taken as a reference.

Clearly, the calculations with pairing correlations reproduce the experimental data well. When the pairing correlations are switched off, the deviations between the data and theoretical results emerge. The bandhead energy for the superdeformed (SD) band from the calculations with pairing correlations is about -335 MeV, 10 MeV higher than the ground state. This may be because the ground state of ^{40}Ca calculated by cranking CDFT-SLAP is overbounded. The calculations without pairing correlations overestimate the experimental data by about 3 MeV at $I = 0\hbar$. The calculations without pairing correlations are consistent with the CRMF results [3]. It is seen that pairing correlations are important for the states with $I \leqslant 10\hbar$ in reproducing the data. With increasing rotational frequency, the results with pairing become closer to those without pairing. Therefore, pairing correlations are important in reproducing the experimental energy spectra, especially for the low-spin regions.

To show the pairing effects more directly, the neutron and proton pairing energies as functions of spin are shown in Fig. 5(b). As can be seen, both the neutron and proton pairing energies change smoothly from about -4 MeV at $I = 0\hbar$ to

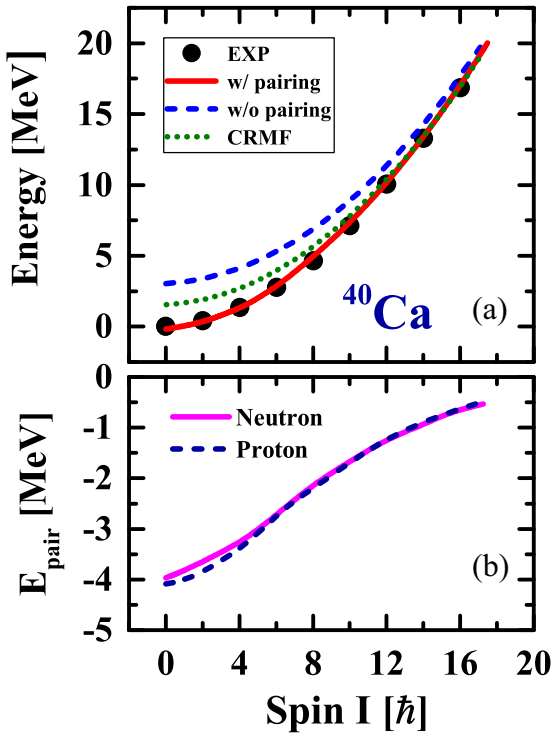

FIG. 5. The energy spectra calculated by the cranking CDFT-SLAP with and without pairing (a) and pairing energies (b) as functions of spin for the SD band in ^{40}Ca. The available data [3] and cranking relativistic mean-field (CRMF) results [3] are also shown for comparison. The $I = 16\hbar$ state is taken as a reference.

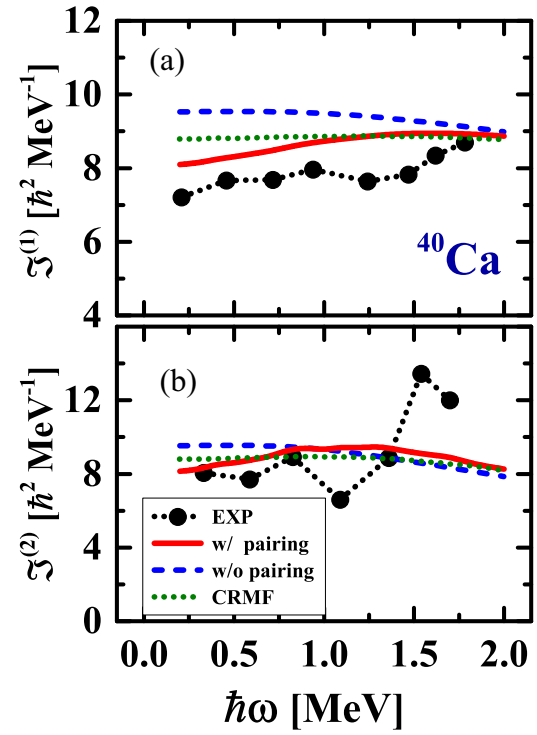

FIG. 6. The kinematic moment of inertia $\Im^{(1)}$ (a) and dynamic moment of inertia $\Im^{(2)}$ (b) as functions of the rotational frequency for the SD band in ^{40}Ca calculated by cranking CDFT-SLAP with and without pairing, in comparison with the available data [3] and cranking relativistic mean-field (CRMF) results [3].

-0.5 MeV at $I = 17\hbar$. The behaviors of the pairing energies as functions of spin for the neutron and proton are similar, since the neutron and proton configurations are the same and the single-particle levels around neutron and proton Fermi levels are similar.

2. *Moments of inertia*

The effects of pairing correlations can be seen more clearly from the moment of inertia (MOI). The kinematic MOI $\Im^{(1)}$ and dynamic MOI $\Im^{(2)}$ are calculated through the following forms:

$$\Im^{(1)} = \frac{\langle\Psi|\hat{J}_x|\Psi\rangle}{\omega}, \quad \Im^{(2)} = \frac{d}{d\omega}\langle\Psi|\hat{J}_x|\Psi\rangle. \tag{8}$$

The calculated kinematic MOI $\Im^{(1)}$ and dynamic MOI $\Im^{(2)}$ with and without pairing correlations are compared with the experimental data and CRMF results in Fig. 6. The experimental $\Im^{(1)}$ and $\Im^{(2)}$ can be extracted from the observed energies of the γ transitions with the following relations [54]:

$$\Im^{(1)}(I) = \frac{2I-1}{E_\gamma(I \to I-2)}\hbar^2\ \text{MeV}^{-1},$$
$$\text{defined at } \hbar\omega = \frac{1}{2}E_\gamma(I \to (I-2))\ \text{MeV} \tag{9}$$

and

$$\Im^{(2)}(I) = \frac{4}{E_\gamma((I+2)\to I) - E_\gamma(I\to(I-2))}\hbar^2\ \text{MeV}^{-1};$$
$$\text{defined at } \hbar\omega = \frac{1}{4}[E_\gamma((I+2)\to I) + E_\gamma(I\to(I-2))]\ \text{MeV}. \tag{10}$$

E_γ is in units of MeV.

For $\Im^{(1)}$, as shown in Fig. 6(a), the experimental data are well reproduced by the calculations with pairing correlations. For the calculations without pairing correlations, the calculated $\Im^{(1)}$ are higher than the data, especially in the low-frequency regions. With increasing rotational frequency, the discrepancies between the calculations with and without pairing correlations are decreased because of the antipairing effect of the Coriolis interaction. The CRMF results are about 5% smaller than the $\Im^{(1)}$ without pairing correlations.

For $\Im^{(2)}$, as shown in Fig. 6(b), the calculations with and without pairing correlations as well as the CRMF results [3] change smoothly with rotational frequency. The experimental data are oscillating with rotational frequency; this may come from the configuration mixing with the normal deformed band [3].

3. *Transition quadrupole moments*

Another important aspect is the transition characters. In Fig 7, the calculated transition quadrupole moment Q_t (a)

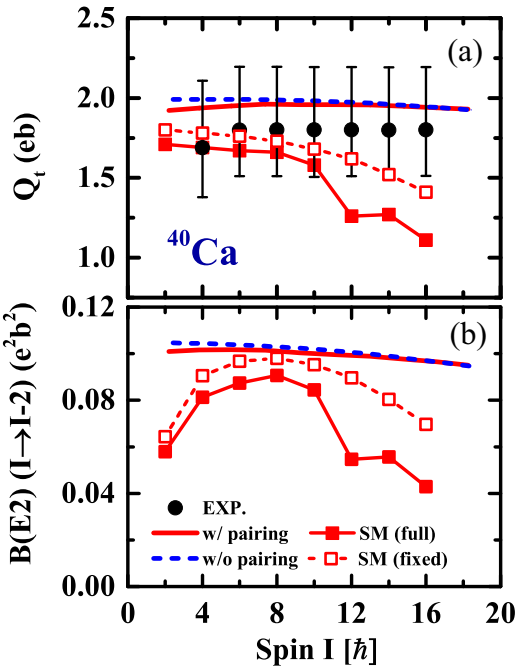

FIG. 7. The transition quadrupole moment Q_t (a) and $B(E2)$ transition probabilities as functions of spin for the SD band in ^{40}Ca calculated by cranking CDFT-SLAP with and without pairing, in comparison with the available data [3,55,56] and the large-scale SM [16] results. The SM (full) in the legend means the SM calculations in the full r_2pf space, while SM (fixed) means the SM calculations in the r_2pf valence space at fixed 8p8h configuration.

and $B(E2)$ (b) transition probabilities are compared with the available data [3,55,56] and large-scale SM calculations [16].

In Fig. 7(a), it can be seen that the cranking CDFT-SLAP calculations without pairing predict a nearly constant Q_t, around 2.0 eb, with increasing spin. The cranking CDFT-SLAP reproduces the available data well within the large experimental error bars. When taking pairing correlations into account, the Q_t values at low spin are decreased, since the pairing correlations reduce the quadrupole deformation. The agreement between the calculations with pairing correlations and the experimental data is improved, especially the increasing behavior from $I = 4\hbar$ to $I = 6\hbar$. However, both results are higher than the center values of experimental data. This indicates that the cranking CDFT-SLAP calculations predict larger deformation. Unlike the results from cranking CDFT-SLAP, a quickly decreasing behavior is seen in the large-scale SM calculations with a fixed $n\hbar\omega$, i.e., SM (fixed), while a large reduction of the transition quadrupole moments of the three upper transitions is seen in the SM (full) calculations. The agreement between the measured data and results from cranking CDFT-SLAP and SM (fixed) calculations suggests that the SD band is of rather pure 8p8h character.

In Fig. 7(b), the $B(E2)$ transition probabilities of the SD band in ^{40}Ca calculated by cranking CDFT-SLAP are compared with the large-scale SM calculations. The cranking CDFT-SLAP calculations predict gradual decreasing trends for the $B(E2)$ values as functions of spin. While trends are much different in the large-scale SM calculation. The $B(E2)$ values increase until $8\hbar$, then decrease. To verify such differences, more experimental data are needed.

V. SUMMARY

In summary, the superdeformed rotational band in the doubly-magic nucleus ^{40}Ca has been investigated in the framework of a shell-model-like approach based on cranking covariant density functional theory, in which the pairing correlations are treated with conserved particle number.

A superdeformed minimum is obtained at the deformation $(\beta,\ \gamma) = (0.70,\ 9^\circ)$ even though the depth of the superdeformed minimum is only about 0.2 MeV. With increasing rotational frequency, the potential around the superdeformed minimum becomes deeper, therefore the superdeformed state becomes more stable. The experimental energy spectra, moments of inertia, as well as the transition quadrupole moments of the superdeformed rotational band in ^{40}Ca are well reproduced by microscopic and self-consistent calculations with pairing correlations. Pairing correlations are important for the states with $I \leqslant 10\hbar$ in the superdeformed rotational band of ^{40}Ca in reproducing the experimental energy spectrum and transition quadrupole moments.

ACKNOWLEDGMENTS

Z.S. is grateful for fruitful discussions with Prof. Jie Meng, Prof. Shuangquan Zhang, Prof. Zhenhua Zhang, and Prof. Pengwei Zhao. We also thank the Sichuan Normal University for financial support (No. 341813001).

[1] P. J. Twin, B. M. Nyakó, A. H. Nelson, J. Simpson, M. A. Bentley, H. W. Cranmer-Gordon, P. D. Forsyth, D. Howe, A. R. Mokhtar, J. D. Morrison *et al.*, Phys. Rev. Lett. **57**, 811 (1986).
[2] B. Singh, R. Zywina, and R. B. Firestone, Nucl. Data Sheets **97**, 241 (2002).
[3] E. Ideguchi, D. G. Sarantites, W. Reviol, A. V. Afanasjev, M. Devlin, C. Baktash, R. V. F. Janssens, D. Rudolph, A. Axelsson, M. P. Carpenter *et al.*, Phys. Rev. Lett. **87**, 222501 (2001).
[4] W. J. Gerace and A. M. Green, Nucl. Phys. A **93**, 110 (1967).
[5] W. J. Gerace and A. M. Green, Nucl. Phys. A **113**, 641 (1968).
[6] M. Bender, H. Flocard, and P. H. Heenen, Phys. Rev. C **68**, 044321 (2003).
[7] H. Röpke, Eur. Phys. J. A **22**, 213 (2004).
[8] D. Vretenar, A. Afanasjev, G. Lalazissis, and P. Ring, Phys. Rep. **409**, 101 (2005).
[9] D. Ray and A. V. Afanasjev, Phys. Rev. C **94**, 014310 (2016).
[10] S. Sakai, K. Yoshida, and M. Matsuo, Prog. Theor. Exp. Phys. **2020**, 063D02 (2020).
[11] T. Inakura, S. Mizutori, M. Yamagami, and K. Matsuyanagi, Nucl. Phys. A **710**, 261 (2002).
[12] E. Caurier, K. Langanke, G. Martinez-Pinedo, F. Nowacki, and P. Vogel, Phys. Lett. B **522**, 240 (2001).

[13] E. Caurier, F. Nowacki, A. Poves, and A. Zuker, arXiv:nucl-th/0205036.
[14] A. Poves, E. Caurier, F. Nowacki, and A. Zuker, Eur. Phys. J. A **20**, 119 (2003).
[15] A. Poves, Nucl. Phys. A **731**, 339 (2004).
[16] E. Caurier, J. Menéndez, F. Nowacki, and A. Poves, Phys. Rev. C **75**, 054317 (2007).
[17] B. G. Dong, H. C. Guo, and Y. J. Shi, Commun. Theor. Phys. **43**, 509 (2005).
[18] Y. Kanada-En'yo and M. Kimura, Phys. Rev. C **72**, 064322 (2005).
[19] Y. Taniguchi, M. Kimura, Y. Kanada-En'yo, and H. Horiuchi, Phys. Rev. C **76**, 044317 (2007).
[20] K. Yoshida, M. Yamagami, and K. Matsuyanagi, Prog. Theor. Phys. **113**, 1251 (2005).
[21] T. Inakura, H. Imagawa, Y. Hashimoto, S. Mizutori, M. Yamagami, and K. Matsuyanagi, Nucl. Phys. A **768**, 61 (2006).
[22] H. Ogasawara, K. Yoshida, M. Yamagami, S. Mizutori, and K. Matsuyanagi, Prog. Theor. Phys. **121**, 357 (2009).
[23] M. Oi, Phys. Rev. C **76**, 044308 (2007).
[24] G. Royer, C. Bonilla, and R. A. Gherghescu, Phys. Rev. C **65**, 067304 (2002).
[25] J. Y. Zeng and T. S. Cheng, Nucl. Phys. A **405**, 1 (1983).
[26] J. Meng, J. Y. Guo, L. Liu, and S. Q. Zhang, Front. Phys. China. **1**, 38 (2006).
[27] J. Y. Zeng, Y. A. Lei, T. H. Jin, and Z. J. Zhao, Phys. Rev. C **50**, 746 (1994).
[28] X. H. Xiang and X. T. He, Chin. Phys. C **42**, 054105 (2018).
[29] S. X. Liu, J. Y. Zeng, and E. G. Zhao, Phys. Rev. C **66**, 024320 (2002).
[30] X. T. He, S. X. Liu, S. Y. Yu, J. Y. Zeng, and E. G. Zhao, Euro. Phys. J. A **23**, 217 (2005).
[31] X. Wu, Z. H. Zhang, J. Y. Zeng, and Y. A. Lei, Phys. Rev. C **83**, 034323 (2011).
[32] Z. H. Zhang, P. W. Zhao, J. Meng, J. Y. Zeng, E. G. Zhao, and S. G. Zhou, Phys. Rev. C **87**, 054314 (2013).
[33] Z. H. Zhang, Phys. Rev. C **94**, 034305 (2016).
[34] S. X. Liu, J. Y. Zeng, and L. Yu, Nuc. Phys. A **735**, 77 (2004).
[35] Z. H. Zhang, X. Wu, Y. A. Lei, and J. Y. Zeng, Nucl. Phys. A **816**, 19 (2009).
[36] Z. H. Zhang, Y. A. Lei, and J. Y. Zeng, Phys. Rev. C **80**, 034313 (2009).
[37] B. H. Li, Z. Z. H. Zhang, and Y. A. Lei, Chin. Phys. C **37**, 014101 (2013).
[38] Y. C. Li and X. T. He, Sci. China Phys. Mech. **59**, 672011 (2016).
[39] Z. H. Zhang, Nucl. Phys. A **949**, 22 (2016).
[40] Z. H. Zhang, J. Meng, E. G. Zhao, and S. G. Zhou, Phys. Rev. C **87**, 054308 (2013).
[41] X. T. He, Z. Z. Ren, S. X. Liu, and E. guang Zhao, Nucl. Phys. A **817**, 45 (2009).
[42] Z. H. Zhang, J. Y. Zeng, E. G. Zhao, and S. G. Zhou, Phys. Rev. C **83**, 011304(R) (2011).
[43] Z. H. Zhang, X. T. He, J. Y. Zeng, E. G. Zhao, and S.-G. Zhou, Phys. Rev. C **85**, 014324 (2012).
[44] Z. H. Zhang, Phys. Rev. C **98**, 034304 (2018).
[45] L. Liu, Z. H. Zhang, and P. W. Zhao, Phys. Rev. C **92**, 044304 (2015).
[46] Z. Shi, Z. H. Zhang, Q. B. Chen, S. Q. Zhang, and J. Meng, Phys. Rev. C **97**, 034317 (2018).
[47] L. Liu, Phys. Rev. C **99**, 024317 (2019).
[48] P. W. Zhao, Z. P. Li, J. M. Yao, and J. Meng, Phys. Rev. C **82**, 054319 (2010).
[49] P. W. Zhao, J. Peng, H. Z. Liang, P. Ring, and J. Meng, Phys. Rev. C **85**, 054310 (2012).
[50] W. Koepf and P. Ring, Nucl. Phys. A **493**, 61 (1989).
[51] K. Kaneko, M. Nakano, and M. Matsuzaki, Phys. Lett. B **317**, 261 (1993).
[52] J. König and P. Ring, Phys. Rev. Lett. **71**, 3079 (1993).
[53] J. Y. Zeng, T. H. Jin, and Z. J. Zhao, Phys. Rev. C **50**, 1388 (1994).
[54] A. V. Afanasjev, D. B. Fossan, G. J. Lane, and I. Ragnarsson, Phys. Rep. **322**, 1 (1999).
[55] J. L. Wood, K. Heyde, W. Nazarewicz, M. Huyse, and P. Van Duppen, Phys. Rep. **215**, 101 (1992).
[56] C. J. Chiara, E. Ideguchi, M. Devlin, D. R. LaFosse, F. Lerma, W. Reviol, S. K. Ryu, D. G. Sarantites, C. Baktash, A. Galindo-Uribarri *et al.*, Phys. Rev. C **67**, 041303(R) (2003).